JOURNAL OF APPLIED CRYSTALLOGRAPHY

ISSN: 1600-5767

journals.iucr.org/j

High-temperature dynamic octahedral tilting in the ionic conductor $Sr_{11}Mo_4O_{23}$

Carlos A. López, José C. Pedregosa, María T. Fernández-Díaz and José A. Alonso

J. Appl. Cryst. (2016). **49**, 78–84

JOURNAL OF APPLIED CRYSTALLOGRAPHY

ISSN 1600-5767

High-temperature dynamic octahedral tilting in the ionic conductor $Sr_{11}Mo_4O_{23}$

Carlos A. López,[a]* José C. Pedregosa,[a] María T. Fernández-Díaz[b] and José A. Alonso[c]

[a]INTEQUI-CONICET and Área de Química General e Inorgánica 'Dr G. F. Puelles', Facultad de Química, Bioquímica y Farmacia, Universidad Nacional de San Luis, Chacabuco y Pedernera, 5700 San Luis, Argentina, [b]Institut Laue-Langevin, BP 156, 38042 Grenoble Cedex 9, France, and [c]Instituto de Ciencia de Materiales de Madrid, CSIC, Cantoblanco, 28049 Madrid, Spain. *Correspondence e-mail: calopez@unsl.edu.ar

Received 7 October 2015
Accepted 25 November 2015

Edited by G. Kostorz, ETH Zurich, Switzerland

Keywords: $Sr_{11}Mo_4O_{23}$; high-temperature structure; neutron powder diffraction; ionic conductors; fuel cells.

Supporting information: this article has supporting information at journals.iucr.org/j

This work presents the crystal structure evolution of a novel ionic conductor $Sr_{11}Mo_4O_{23}$ at high temperature. The formula of this phase can be rewritten as $Sr_{1.75}\square_{0.25}SrMoO_{5.75}$, highlighting the relationship with double perovskites $A_2B'B''O_6$. The crystal network contains oxygen-anion and strontium-cation vacancies. The structure is complex; Sr, Mo and O atoms are distributed in four, two and six distinct Wyckoff sites, respectively. It was refined from neutron powder diffraction data collected at 473, 673, 873 and 1073 K. The thermal evolution of crystallographic parameters supports the known reversible process of removal/uptake of O-atom content in the 673–873 K temperature range. Above 873 K, from difference Fourier maps, it was found that the structure exhibits an oxygen delocalization around one of the Mo sites. This delocalization was understood as a dynamical octahedral tilt of the MoO_6 octahedron, yielding an increase in the ionic conductivity at high temperature.

1. Introduction

Transition-metal oxides are currently of significant interest for the development of renewable energy technologies such as solid oxide fuel cells (SOFCs), thermoelectric modules and high-temperature superconductors (Rao & Raveau, 1998; Raveau, 2007). SOFCs have been recognized as promising energy generation devices, which convert chemical energy of fuel directly into electricity with high efficiency and fuel flexibility (Singhal, 2000). These electrochemical devices can be operated with a variety of different fuels, such as hydrogen, syngas, natural gas, biogas or even solid carbon (Jiang *et al.*, 2006; Jin *et al.*, 2012). However, several issues have to be solved in order to improve their efficiency and in terms of costs of operation.

The reduction of the typically high working temperature, which is around 1173–1273 K, is one of the most important issues, in order to avoid degradation problems due to thermal cycling or diffusion at interfaces and to reduce the cost of the interconnection materials. For this reason, extensive research has been devoted in recent years to the study of novel materials and structures able to outperform intermediate-temperature SOFCs in the 923–1073 K range. Besides electrode materials, novel solid oxide electrolytes need to be identified, with enhanced oxygen diffusion properties at such low temperatures. In oxide-ion conductors, current flow occurs by the movement of oxygen ions through the crystal lattice as a result of thermally activated hopping of the oxygen ions moving from a crystal lattice site to adjacent vacancies or interstitial positions. Typical commercially available materials

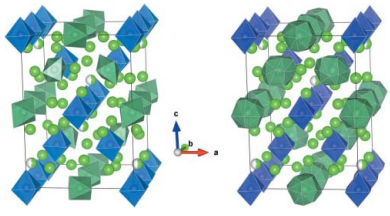

are related to the fluorite structure, like YSZ (Badwal, 1992) and GDC (Steele, 2000) (with compositions $Zr_{1-x}Y_xO_{2-\delta}$ and $Ce_{1-x}GdO_{2-\delta}$). As an alternative to fluorite, some perovskite-type oxides showing oxygen sub-stoichiometry (allowing an oxygen-vacancy conduction mechanism) have been explored, like those based on the $LaGaO_3$ system (with composition $La_{1-x}Sr_xGa_{1-y}Mg_yO_{3-\delta}$, known as LSGM materials; Ishihara *et al.*, 1994; Feng & Goodenough, 1994; Huang *et al.*, 1998; Tao *et al.*, 2005).

More complex perovskite systems, like double perovskite ($A_2B'B''O_6$) oxides, may also find applications in the energy conversion field. These systems are derived from the simple ABO_3 perovskite structure by the introduction of two *B*-site cations arranged in a rock-salt fashion. Some of these materials have an ideal cubic structure, while most present distortions or deviations of the canonical stoichiometry. The most common are the octahedral tilting distortions, sometimes combined with vacancies at both *A* sites and O sites. An exceptional example of the flexibility of the perovskite framework is the family of composition $A_{1.75}\square_{0.25}B'B''O_6$ (where $A = B'$ and $\square$ = vacancy at the *A* sublattice); the structure is able to accommodate a rotation of 50% of the small $B''O_6$ octahedra by $\sim 45^\circ$ so that the coordination number of all B' cations is raised to eight. The known compounds with this structure are $Sr_{11}Os_4O_{24}$, $Ca_{11}Re_4O_{24}$, $Sr_{11}Re_4O_{24}$ and $Ba_{11}Os_4O_{24}$ (Tomaszewska & Müller-Buschbaum, 1993; Jeitschko *et al.*, 1998; Bramnik *et al.*, 2000; Wakeshima & Hinatsu, 2005). A few years ago, a new perovskite with this structure was reported where *A*-site deficiency is observed together with oxygen vacancies ($Ba_{11}W_4O_{23}$ or $Ba_{1.75}\square_{0.25}BaWO_{5.75}\square_{0.25}$; Hong, 2007; Ha *et al.*, 2008).

Recently, we have prepared and studied a novel Mo-containing related framework with a strongly defective $A_{11}B_4O_{23}$ stoichiometry (López *et al.*, 2014). This material, $Sr_{11}Mo_4O_{23}$, performs as an oxide-ion conductor, with a moderate ionic conductivity compared with the conventional electrolyte oxides, but it opens up new possibilities on where to search for novel electrolyte materials. It exhibits a reversible process of removal/uptake of O-atom content in the 673–873 K temperature range. This change is observed by thermogravimetric analysis, by differential scanning calorimetry and in the thermal expansion. The conductivity is strongly activated after the topotactic removal of 0.54 O atoms per formula unit (López *et al.*, 2014). In the present work we complete the characterization of this oxide by describing the thermal evolution of the complex crystal structure at high temperature, studied *in situ* by neutron powder diffraction (NPD). We also interpret the strongest increase in the ionic conductivity in relation to the crystal structure features observed at high temperature.

2. Experimental

$Sr_{11}Mo_4O_{23}$ was prepared as a brown polycrystalline powder from citrate precursors obtained by soft chemistry procedures, as previously reported (López *et al.*, 2014). The initial identification and characterization of the sample was carried out by X-ray powder diffraction. The experimental patterns were obtained on a Rigaku D-MAX-IIIC diffractometer with Cu $K\alpha$ (λ = 1.5418 Å) radiation. To study the crystallographic structure at high temperature (473, 673, 873 and 1073 K), NPD patterns were collected on the D2B diffractometer at ILL (Institute Laue–Langevin, Grenoble, France) with a wavelength of 1.549 Å. NPD diffraction patterns were refined with the Rietveld method using the *FullProf* program (Rietveld, 1969; Rodríguez-Carvajal, 1993).

3. Results and discussion

3.1. Structure at room temperature

The structural refinement at room temperature was previously performed and reported from combined X-ray powder diffraction and NPD data (López *et al.*, 2014). At room temperature, this compound exhibits a cation-deficient structure where the corner-sharing connectivity of the octahedral framework is broken.

The distorted double perovskites with broken corner-sharing connectivity of the octahedral framework are mostly *A*-site-deficient mixed oxides. Accordingly, this formula can be rewritten as $Sr_7\square(Sr_4Mo_4)O_{23}\square$ or as a double perovskite: $Sr_{1.75}\square_{0.25}(SrMo)O_{5.75}\square_{0.25}$. The oxygen content of 5.75 was computed from the charge balance of the compound assuming that Mo is hexavalent. The structure may be regarded as a cation-vacancy-ordered double perovskite structure, forming a novel superstructure.

This superstructure presents a tetragonal symmetry ($I4_1/a$) where the cell parameters are connected with the parameter of the simple cubic perovskite ABO_3 (a_0) as $a = b \simeq 2(2^{1/2})a_0$; $c \simeq 4a_0$. For this crystallographic model the strontium atoms are distributed at four different positions, molybdenum at two and oxygen at six. Three Sr sites (Sr1, Sr2 and Sr3) correspond to *A*-site cations exhibiting different coordinations ranging from 12 to 8, while one Sr and two Mo sites (Sr4, Mo1 and Mo2) correspond to *B*-site cations.

3.2. Structure at high temperature

The thermal evolution of the crystal structure was evaluated by NPD. For this purpose, the sample was contained in a vanadium can under high vacuum (10^{-6} Torr; 1 Torr $\simeq$ 133 Pa) and NPD data were collected *in situ* in a furnace at 473, 673, 873 and 1073 K. The NPD patterns show no structural phase transition within the temperature range under study (298–1073 K). Fig. 1 shows the thermal evolution of the unit-cell volume. This plot indicates a linear increase of the unit-cell volume up to 675 K; however, at 873 and 1073 K these parameters are above linear extrapolation. From this behaviour we can estimate the thermal expansion coefficient as 12.4 and 16.6×10^{-6} K^{-1} in the temperature ranges 298–673 and 873–1073 K, respectively. These values are in accord with those previously obtained by us from dilatometry measurements (14.8 and 17.0 $\times$ 10^{-6} K^{-1} at low and high temperatures, respectively; López *et al.*, 2014). This change was previously

Table 1
Crystallographic data for the $Sr_{11}Mo_4O_{23}$ phase from the NPD refinements at 473 K.

System: tetragonal; space group: $I4_1/a$; Z = 4. Unit-cell parameters: a = 11.6416 (4), c = 16.4524 (9) Å and V = 2229.7 (2) Å^3.

Atom		x	y	z	B_{iso}	Occ
Sr1	4*a*	0	0.25	0.125	3.5 (4)	1
Sr2	8*e*	0.5	0.25	0.601(2)	4.7 (5)	1
Sr3	16*f*	0.224 (1)	0.976 (1)	0.877 (1)	2.6 (2)	1
Sr4	16*f*	0.212 (1)	0.238 (1)	0.529 (1)	4.1 (2)	1
Mo1	8*c*	0	0	0	0.7 (1)	1
Mo2	8*d*	0	0	0.5	3.6 (2)	1
O1	16*f*	−0.115 (1)	−0.120 (1)	0.007 (1)	2.5 (3)	1
O2	16*f*	0.124 (1)	−0.115 (1)	0.008 (1)	2.4 (3)	1
O3	16*f*	−0.004 (1)	0.020 (2)	0.117 (1)	1.8 (2)	1
O4	16*f*	0.084 (1)	0.080 (1)	0.595 (1)	1.7 (3)	0.78 (2)
O5	16*f*	0.120 (1)	−0.083 (1)	0.493 (1)	3.7 (3)	1
O6	16*f*	−0.095 (1)	−0.062 (1)	0.570 (1)	4.4 (3)	1

NPD: R_p: 3.2%; R_{wp}: 4.4%; R_{exp}: 1.2%; χ^2: 12.8; R_{Bragg}: 8.6%.

Table 2
Crystallographic data for the $Sr_{11}Mo_4O_{23}$ phase from the NPD refinements at 673 K.

System: tetragonal; space group: $I4_1/a$; Z = 4. Unit-cell parameters: a = 11.6696 (4), c = 16.4869 (9) Å and V = 2245.2 (2) Å^3.

Atom		x	y	z	B_{iso}	Occ
Sr1	4*a*	0	0.25	0.125	4.3 (6)	1
Sr2	8*e*	0.5	0.25	0.603 (1)	7.2 (6)	1
Sr3	16*f*	0.234 (1)	0.972 (1)	0.880 (1)	3.2 (2)	1
Sr4	16*f*	0.220 (1)	0.233 (1)	0.534 (1)	5.0 (3)	1
Mo1	8*c*	0	0	0	2.4 (2)	1
Mo2	8*d*	0	0	0.5	2.4 (2)	1
O1	16*f*	−0.121 (1)	−0.111 (1)	0.001(1)	2.4 (2)	1
O2	16*f*	0.113 (1)	−0.117 (2)	0.009 (1)	3.0 (4)	1
O3	16*f*	−0.004 (1)	0.022 (1)	0.118 (1)	2.2 (2)	1
O4	16*f*	0.080 (2)	0.089 (1)	0.593 (1)	3.2 (4)	0.79 (2)
O5	16*f*	0.124 (1)	−0.090 (2)	0.494 (1)	6.1 (5)	1
O6	16*f*	−0.092 (2)	−0.076 (3)	0.565 (1)	9.6 (7)	1

NPD: R_p: 2.9%; R_{wp}: 3.9%; R_{exp}: 1.2%; χ^2: 9.8; R_{Bragg}: 8.1%.

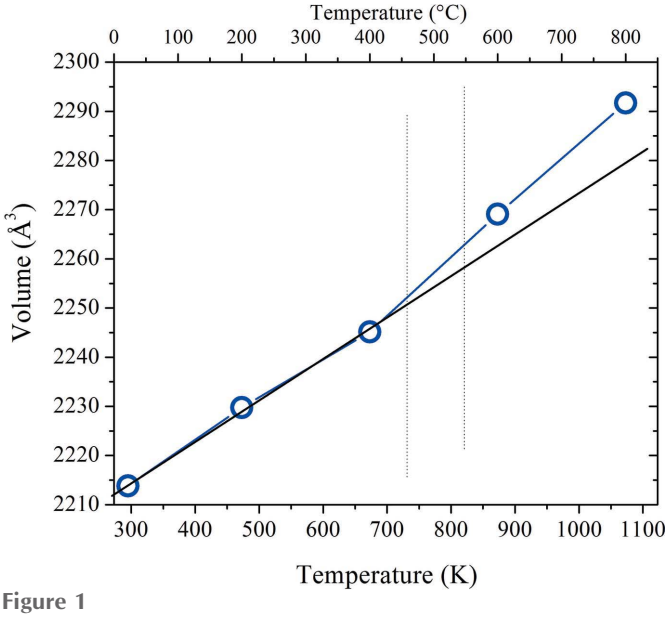

Figure 1
Thermal evolution of unit-cell volume. The black solid line indicates the linear regression from room temperature to 673 K.

attributed to a reversible process of removal/uptake of O-atom content in the 673–873 K temperature range. Keeping these data in mind, we refined and analysed the crystal structure below (473 and 673 K) and above (873 and 1073 K) the previously observed reversible change.

Fig. 2 illustrates the good agreement between the observed and calculated NPD patterns for $Sr_{11}Mo_4O_{23}$ at 473 and 673 K. Tables 1 and 2 summarize the results obtained from the refinements at both temperatures. In both cases, some minor impurity phases were identified and included in the refinement: $SrMoO_4$ (space group $I4_1/a$) (also observed in X-ray powder diffraction), $Sr(OH)_2{\cdot}H_2O$ (space group $Pmc2_1$) and SrO (space group $I4/mmm$) (Guermen *et al.*, 1971; Kuske *et al.*,

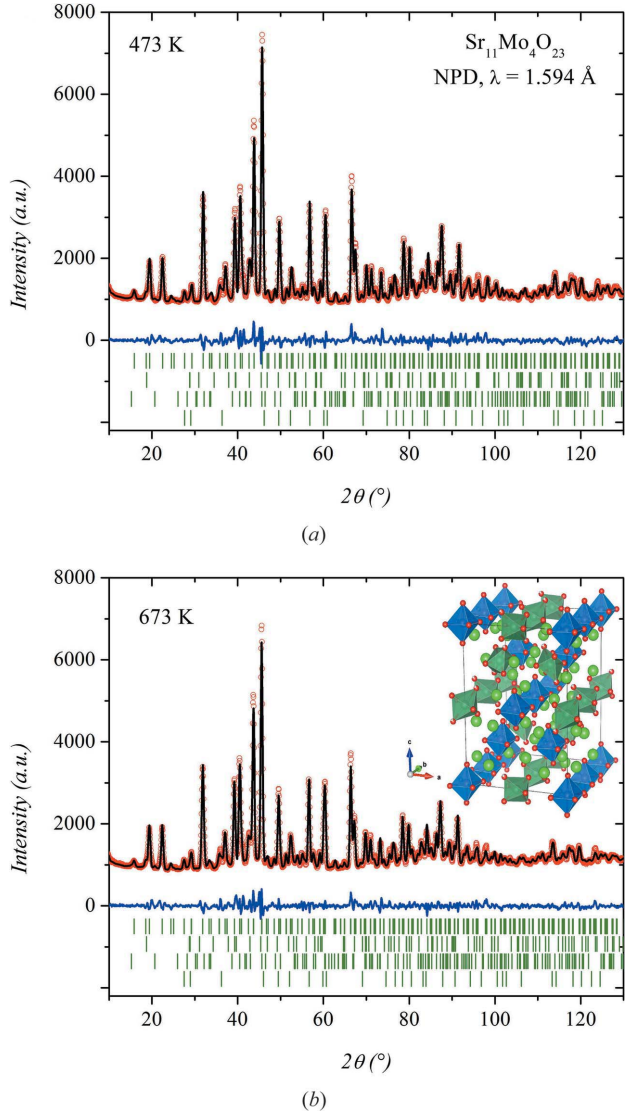

Figure 2
Neutron powder diffraction data (circles) and Rietveld calculated line profiles (full line) for the $Sr_{11}Mo_4O_{23}$ complex perovskite at (*a*) 473 K and (*b*) 673 K. The line at the bottom is the difference between the calculated and experimental patterns. The upper set of bars correspond to the Bragg reflections for the main phase and the lower sets of bars correspond to the Bragg reflections for the impurity phases: $SrMoO_4$, $Sr(OH)_2{\cdot}H_2O$ and SrO. The inset in (*b*) is a schematic view of the crystal structure showing the $Mo1O_6$ (blue) and $Mo2O_6$ (green) octahedra and the Sr atoms (green spheres).

1988; Bashir *et al.*, 2002). From the scale factors of the main and secondary phases, the different impurities were found to account for less than 2% in weight. These impurities arise as a consequence of the superficial hydration process observed previously from thermogravimetric analysis and infrared spectroscopy (López *et al.*, 2014), and disappear upon heating the sample as described below.

The crystal structures at 473 and 673 K are similar to that reported at room temperature (RT), where the Mo1, Mo2 and Sr4 atoms occupy the *B* positions of the perovskite subcell in an ordered manner, forming a 'rock-salt'-type cation sublattice. The Mo1 and Mo2 ions are coordinated by six oxide ions, forming MoO_6 octahedra, whereas the Sr4 ion is coordinated by eight O atoms, forming SrO_8 polyhedra. These polyhedra link with six neighbouring MoO_6 octahedra in a three-dimensional network by corner sharing and edge sharing. In order to incorporate the SrO_8 polyhedra, the perovskite octahedral framework is significantly transformed. The $Mo1O_6$ octahedra are only slightly tilted along [110], whereas the $Mo2O_6$ octahedra are rotated along the same axis by ∼45°. A schematic view of the crystallographic structure is shown in the inset of Fig. 2(*b*).

As can be seen in Tables 1 and 2, the occupation of the atom O4 showed a deficit of 22 (2) and 21 (2)% at 473 and 673 K, respectively, and the O atoms of the equatorial plane also exhibit very large displacement factors. These crystallographic features are similar to those previously observed at RT, showing that this material has a regular thermal evolution, in agreement with dilatometric measurements and conductivities observed up to 673 K (López *et al.*, 2014).

The NPD data at 873 and 1073 K do not show structural changes with respect to those recorded at lower temperatures. However, these patterns show that the impurity reflections disappear and the background intensity decreases. Both effects are directly related to the superficial dehydration of the sample in the furnace, which has already been observed from thermogravimetric analysis and infrared spectroscopy (López *et al.*, 2014). Both diagrams correspond now to the pure perovskite single phase.

On the other hand, despite the fact that Bragg positions were correctly fitted, suggesting the same space group, selected diffraction patterns show discrepancies in the intensity fit, producing poor agreement factors. The major contributions to these selected reflections are given by the O atoms

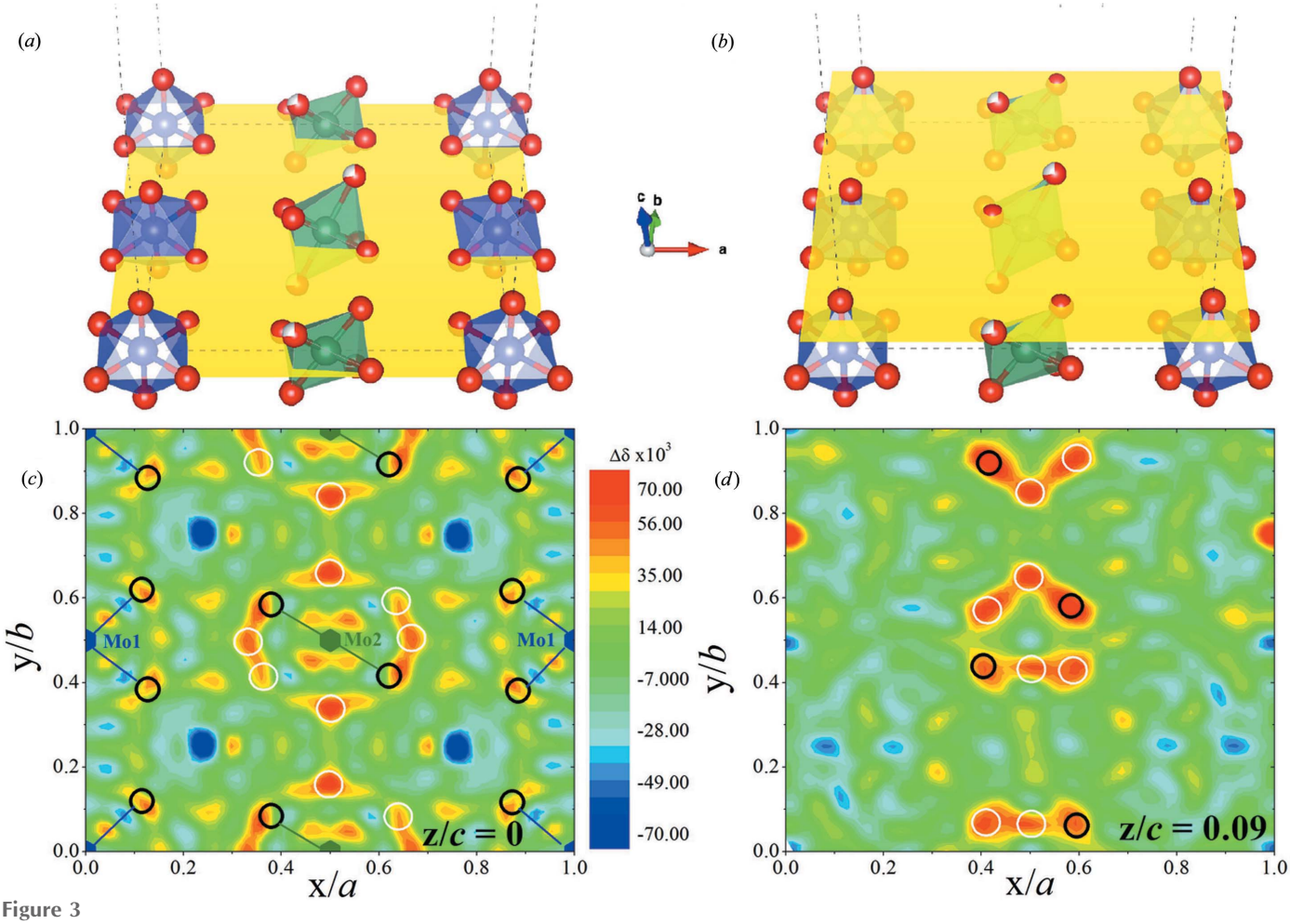

Figure 3
(Top) A schematic view of the crystallographic planes (001) at (*a*) $z/c = 0$ and (*b*) $z/c = 0.09$ where the nuclear density is analysed. (Bottom) Difference Fourier maps in the planes (001) at (*c*) $z/c = 0$ and (*d*) $z/c = 0.09$. Blue and green hexagons indicate the Mo1 and Mo2 positions, respectively. The open black circles indicate the equivalent oxygen positions at room temperature and the white circles are the newfound oxygen positions.

bonded to Mo2 (O4, O5 and O6), which were proposed as being responsible of the O^{2-} mobility in this compound. Also the O4, O5 and O6 positions and ⟨Mo2—O⟩ distances obtained from the refinement were unrealistic.

In order to analyse and retrieve the oxygen positions around Mo2, we examined the nuclear density in the crystallographic planes where the O atoms with wrong interatomic distances are located [(001) plane at z/c = 0 and 0.09]; these planes are illustrated in Figs. 3(*a*) and 3(*b*), respectively. This analysis was carried out from difference Fourier maps (DFMs) obtained from the *GFourier* program (Gonzalez-Platas & Rodriguez-Carvajal, 2007). These maps show the difference between the observed and calculated nuclear densities, where we have eliminated the uncertain atoms (O4, O5 and O6). Figs. 3(*c*) and 3(*d*) show the DFMs in the (001) planes at z/c = 0 and 0.09, respectively. In the colour scale, the red colour shows positive nuclear density in the observed pattern, absent in the calculated pattern, and the blue colour indicates negative nuclear density. In the picture the blue and green hexagonal symbols correspond to Mo1 and Mo2 atoms, respectively; the black circles correspond to the O atoms according to the room-temperature structure.

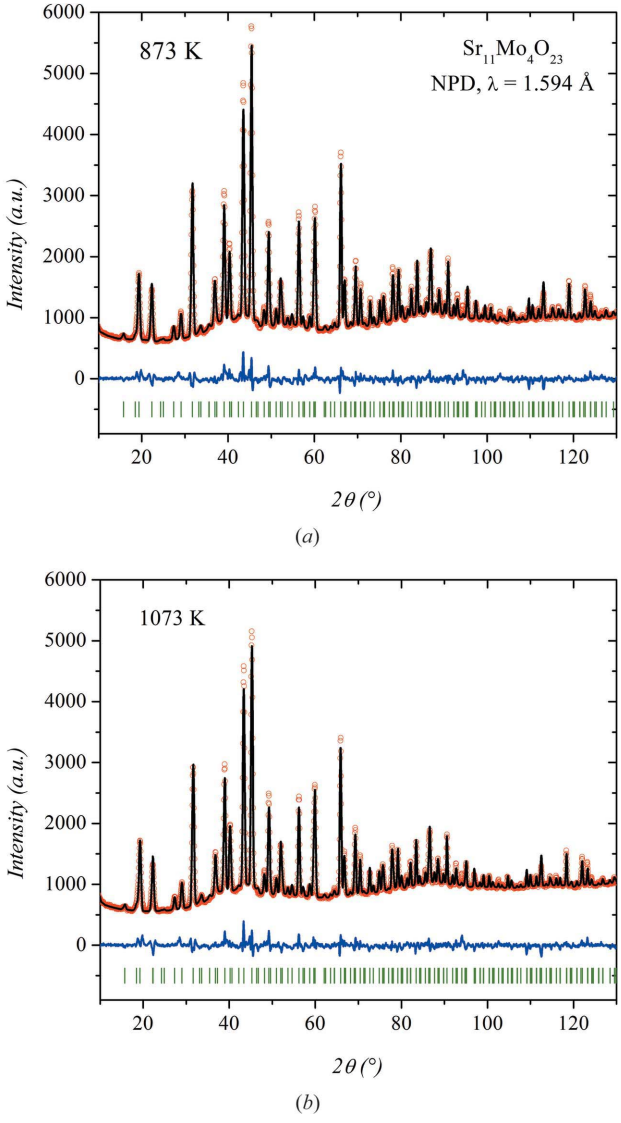

Figure 4
Neutron powder diffraction data (circles) and Rietveld calculated line profiles (full line) for the $Sr_{11}Mo_4O_{23}$ complex perovskite at (*a*) 873 K and (*b*) 1073 K. The line at the bottom is the difference between calculated and experimental patterns. The set of bars correspond to the Bragg reflections for the crystal structure.

Table 3
Crystallographic data for the $Sr_{11}Mo_4O_{23}$ phase from the NPD refinements at 873 K.

System: tetragonal; space group: $I4_1/a$; Z = 4. Unit-cell parameters: a = 11.7075 (3), c = 16.5548 (8) Å and V = 2269.1 (1) Å^3.

Atom		x/a	y/b	z/c	B_{iso}	Occ
Sr1	4*a*	0	0.25	0.125	5.9 (5)	1
Sr2	8*e*	0.5	0.25	0.602 (2)	4.5 (5)	1
Sr3	16*f*	0.226 (2)	0.980 (2)	0.873 (1)	4.4 (3)	1
Sr4	16*f*	0.209 (2)	0.246 (3)	0.527 (1)	5.5 (2)	1
Mo1	8*c*	0	0	0	2.1 (1)	1
Mo2	8*d*	0	0	0.5	2.7 (2)	1
O1	16*f*	0.877 (2)	0.147 (2)	0.253 (1)	3.9 (3)	1
O2	16*f*	0.643 (1)	0.126 (1)	0.246 (1)	2.4 (2)	1
O3	16*f*	0.263 (2)	0.243 (2)	0.366 (2)	4.4 (3)	1
O4a	16*f*	−0.086 (1)	−0.055 (2)	0.412 (2)	3.0†	0.30 (2)
O4b	16*f*	−0.087 (2)	0.094 (2)	0.425 (3)	3.0†	0.13 (3)
O4c	16*f*	0.000 (2)	0.072 (2)	0.400 (2)	3.0†	0.30 (2)
O5a	16*f*	0.132 (3)	−0.094 (3)	0.490 (3)	3.0†	0.30 (2)
O5b	16*f*	−0.137 (3)	−0.087 (3)	0.485 (3)	3.0†	0.30 (2)
O5c	16*f*	−0.163 (2)	0.005 (4)	0.478 (3)	3.0†	0.30 (2)
O5d	16*f*	0.000 (9)	−0.170 (2)	0.500 (4)	3.0†	0.18 (2)
O6a	16*f*	0.087 (2)	0.060 (2)	0.412 (2)	3.0†	0.30 (2)
O6b	16*f*	0.086 (1)	−0.082 (3)	0.409 (2)	3.0†	0.22 (2)
O6c	16*f*	0.000 (4)	−0.148 (2)	0.435 (2)	3.0†	0.13 (1)

NPD: R_p: 2.8%; R_{wp}: 3.9%; R_{exp}: 1.4%; χ^2: 8.6; R_{Bragg}: 11.1%. † Constrained parameters, see text.

From the DFM in Fig. 3(*c*), we can observe that the $Mo1O_6$ octahedra are correctly placed and no substantial differences are observed. However, as noted above, the uncertain atoms are the O atoms linked to Mo2, where the open black circles correspond to the room-temperature positions for the O5 atoms. These oxygen positions are close to a positive nuclear density, but it is not the only one located around Mo2. In Fig. 3(*c*) it is possible to observe at least six more positive density zones (highlighted with open white circles) around Mo2 in the plane (001). We can assign these positive densities to eight atoms, corresponding to four new crystallographic oxygen positions, in this plane. The two other O atoms of the $Mo2O_6$ octahedron are close to the same plane, but at z/c = 0.09 (see Figs. 3*b* and 3*d*). A similar situation is observed in this plane, where four new positive densities appear. Despite the appearance of several positive density regions surrounding the Mo2 atoms, in most cases these densities are moderate, which may suggest that these positions have low occupancy factors.

Considering the DFMs and the ionic conductivity of this material, we can think of the crystal structure as exhibiting a delocalization of the oxygen positions around Mo2. This delocalization can also be viewed as a dynamical tilting of the $Mo2O_6$ octahedron around the z axis. According to the DFM,

Table 4
Crystallographic data for the $Sr_{11}Mo_4O_{23}$ phase from the NPD refinements at 1073 K.

System: tetragonal; space group: $I4_1/a$; Z = 4. Unit-cell parameters: a = 11.7466 (3), c = 16.6088 (8) Å and V = 2291.7 (1) Å^3.

Atom		x/a	y/b	z/c	B_{iso}	Occ
Sr1	4*a*	0	0.25	0.125	6.4 (5)	1
Sr2	8*e*	0.5	0.25	0.600 (2)	4.5 (5)	1
Sr3	16*f*	0.227 (2)	0.976 (2)	0.874 (1)	4.9 (3)	1
Sr4	16*f*	0.207 (2)	0.246 (3)	0.528 (2)	6.6 (2)	1
Mo1	8*c*	0	0	0	2.5 (1)	1
Mo2	8*d*	0	0	0.5	2.9 (2)	1
O1	16*f*	0.875 (2)	0.145 (2)	0.251 (2)	4.5 (4)	1
O2	16*f*	0.642 (1)	0.127 (2)	0.247 (1)	3.3 (3)	1
O3	16*f*	0.259 (2)	0.242 (2)	0.366 (1)	4.6 (4)	1
O4a	16*f*	−0.084 (1)	−0.047 (2)	0.411 (2)	3.0†	0.30 (2)
O4b	16*f*	−0.085 (2)	0.101 (2)	0.429 (3)	3.0†	0.14 (3)
O4c	16*f*	0.000 (2)	0.076 (2)	0.403 (2)	3.0†	0.30 (2)
O5a	16*f*	0.131 (3)	−0.093 (3)	0.488 (3)	3.0†	0.30 (2)
O5b	16*f*	−0.142 (2)	−0.080 (3)	0.490 (3)	3.0†	0.30 (2)
O5c	16*f*	−0.162 (2)	0.000 (5)	0.477 (3)	3.0†	0.30 (2)
O5d	16*f*	0.000 (9)	−0.170 (2)	0.500 (4)	3.0†	0.15 (2)
O6a	16*f*	0.085 (2)	0.060 (2)	0.412 (2)	3.0†	0.30 (2)
O6b	16*f*	0.084 (1)	−0.081 (2)	0.407 (2)	3.0†	0.21 (2)
O6c	16*f*	0.000 (4)	−0.142 (2)	0.429 (2)	3.0†	0.15 (1)

NPD: R_p: 2.6%; R_{wp}: 3.7%; R_{exp}: 1.4%; χ^2: 7.0; R_{Bragg}: 10.7%. † Constrained parameters, see text.

we found up to ten non-equivalent crystallographic oxygen positions surrounding Mo2 atoms, which are consistent with the proposed octahedron tilt.

In order to model this situation, we replaced O4, O5 and O6 by the mentioned ten oxygen sites. The x, y and z parameters and occupancy factors were refined simultaneously, but the displacement factors were refined as a unique parameter. This crystallographic model leads now to a good agreement between the observed and calculated NPD patterns after the refinements, as is shown in Figs. 4(*a*) and 4(*b*). The most important structural parameters of the crystallographic structure and the discrepancy factors at 873 and 1073 K are listed in Tables 3 and 4, respectively.

From these refinements we can interpret the increase in the conductivity as being concomitant with the delocalization of O atoms around Mo2. The positions of the new O atoms

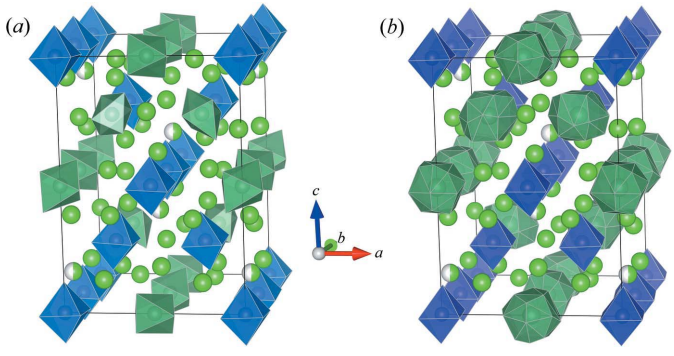

Figure 5
Comparison between the crystallographic structures below (*a*) and above (*b*) the oxygen delocalization process.

Table 5
Oxygen content as a function of temperature.

RT	473 K	673 K	873 K	1073 K
$Sr_{11}Mo_4O_{23.1(2)}$	$Sr_{11}Mo_4O_{23.1(1)}$	$Sr_{11}Mo_4O_{23.2(1)}$	$Sr_{11}Mo_4O_{21.8(2)}$	$Sr_{11}Mo_4O_{21.9(2)}$

converge well during the refinements, and the individual occupancy is less than half in all cases. From these occupancy factors we can calculate the oxygen content for each temperature as shown in Table 5.

From these values we can observe a sudden oxygen loss process between 673 and 873 K. This fact is compatible with the reversible process of removal/uptake of O-atom content previously reported from thermogravimetric analysis (López *et al.*, 2014) at similar temperatures. Fig. 5 shows a schematic view of the crystal structure after and before this reversible process, where the delocalization phenomenon is observed around the Mo2 atoms (green polyhedra). The Mo2 polyhedron observed at 1073 K (or at 873 K), as mentioned above, may be considered as formed by an octahedron dynamically tilted in different directions. This fact can be observed in Fig. 6 where the Mo2 polyhedron (Fig. 6*a*) is decomposed into the three different octahedral frames described in Fig. 6(*b*).

Also in these high-temperature structures the oxygen delocalization produces an improved connectivity between the O atoms of the Mo2 polyhedra. For example, this polyhedron forms chains through atoms O5*d*—O5*d* at a distance of 1.88 Å along the **x** and **y** directions (see Fig. 6*a*). Also, these chains are connected *via* O4*a*—O6*b* at 2.06 Å. These connections generate a three-dimensional network permitting these O atoms to diffuse throughout the crystal structure, accounting for the good oxide-ion conductivity properties.

Finally, it is interesting to compare the behaviour of the present material with that of the already known double perovskites containing molybdenum. For instance, $Sr_2(Mn,Mg)MoO_6$ or $Sr_{2-x}\square_xMgMoO_{6-\delta}$ (with x up to 0.15) oxides were recently described as mixed ionic electronic conductors (MIECs), showing promising properties as anodic materials for SOFCs (Troncoso *et al.*, 2013; Jiang *et al.*, 2014). The different mechanism of conductivity between $Sr_{2-x}MgMoO_6$ (MIEC) and $Sr_{11}Mo_4O_{23}$ (pure ionic conduction) is tightly related to the structural differences and is a result of the broken corner-sharing features observed in $Sr_{11}Mo_4O_{23}$,

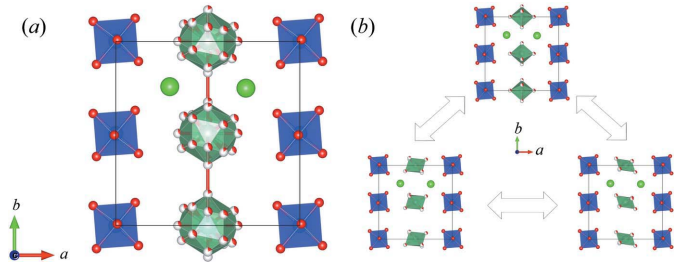

Figure 6
(*a*) A schematic view of the oxygen delocalization around the Mo2 atoms in the (001) plane. (*b*) Decomposition of the Mo2 polyhedron into the octahedral resonant forms.

whereas $Sr_{2-x}MgMoO_6$ has the conventional double perovskite structure with full corner-sharing connectivity.

4. Conclusions

$Sr_{11}Mo_4O_{23}$ oxide is a novel double perovskite with broken corner-sharing connectivity of the octahedral framework. This material has a strong increase of the ionic conductivity activated after the topotactical removal of O atoms above 673 K. The crystallographic features at different temperatures confirm the reversible process of removal/uptake of O-atom content in the 673–873 K temperature range. High-temperature neutron diffraction data also reveal that the loss of oxygen is not the only cause of the increase of conductivity, as discussed in the previous report (López *et al.*, 2014). Above 873 K a strong oxygen delocalization is observed around the Mo2 atoms. This delocalization is modelled as an $Mo2O_6$ octahedron that is dynamically tilting around the *z* axis, adopting different positions. These positions can be considered as the resonant forms of this octahedron in the crystal structure. This crystallographic feature, enabling the delocalization of O atoms and enhancing the connectivity of Mo2 polyhedra across the three crystal directions, unknown until now, is the main cause of the increase in the ionic conductivity. The elucidation of this mechanism of oxide-ion mobility constitutes an interesting starting point for the design of isostructural materials with enhanced ionic conductivity in the development of novel solid electrolytic materials.

Acknowledgements

JCP thanks CONICET [projects PIP 11220080101360-Visita Científica PVCE(CSIC) and PIP 00912/12] and SECyT-UNSL (PROICO 2-1612). CAL acknowledges ANPCyT for financial support (project PICT 2014-3576). CAL and JCP are members of CONICET. JAA thanks the Spanish MINECO for funding the project MAT2013-41099R. We are grateful to ILL for making the neutron beamtime available.

References

Badwal, S. P. S. (1992). *Solid State Ionics*, **52**, 23–32.
Bashir, J., Khan, R. T. A., Butt, N. M. & Heger, G. (2002). *Powder Diffr.* **17**, 222–224.
Bramnik, K. G., Miehe, G., Ehrenberg, H., Fuess, H., Abakumov, A. M., Shpanchenko, R. V., Pomjakushin, V. Y. & Balagurov, A. M. (2000). *J. Solid State Chem.* **149**, 49–55.
Feng, M. & Goodenough, J. B. (1994). *Eur. J. Solid State Inorg. Chem.* **T31**, 663–672.
Gonzalez-Platas, J. & Rodriguez-Carvajal, J. (2007). *GFourier*. Version 4.06. (Included in the *FullProf Suite* package.) Universidad de La Laguna, Tenerife, Spain, and Laboratoire Leon Brillouin, Saclay, France.
Guermen, E., Daniels, E. & King, J. S. (1971). *J. Chem. Phys.* **55**, 1093–1097.
Ha, J.-S., Lee, E., Hong, S.-T. & Yoo, H.-I. (2008). *Solid State Ionics*, **179**, 1066–1070.
Hong, S.-T. (2007). *J. Solid State Chem.* **180**, 3039–3048.
Huang, K., Tichy, R. S., Goodenough, J. B. & Milliken, C. (1998). *J. Am. Ceram. Soc.* **81**, 2581–2585.
Ishihara, T., Matsuda, H. & Takita, Y. (1994). *J. Am. Chem. Soc.* **116**, 3801–3803.
Jeitschko, W., Mons, H. A., Rodewald, U. C. & Möller, M. H. (1998). *Z. Naturforsch. Teil B*, **53**, 31–36.
Jiang, L., Liang, G., Han, J. & Huang, Y. (2014). *J. Power Sources*, **270**, 441–448.
Jiang, S. P., Chen, X. J., Chan, S. H., Kwok, J. T. & Khor, K. (2006). *Solid State Ionics*, **177**, 149–157.
Jin, C., Yang, Z., Zheng, H., Yang, C. & Chen, F. (2012). *Electrochem. Commun.* **14**, 75–77.
Kuske, P., Engelen, B., Henning, J., Lutz, H. D., Fuess, H. & Gregson, D. (1988). *Z. Kristallogr.* **183**, 319–325.
López, C. A., Pedregosa, J. C., Lamas, D. G. & Alonso, J. A. (2014). *J. Appl. Cryst.* **47**, 1395–1401.
Rao, C. N. R. & Raveau, B. (1998). *Transition Metal Oxides: Structure, Properties, and Synthesis of Ceramic Oxides.* New York: John Wiley and Sons.
Raveau, B. (2007). *Prog. Solid State Chem.* **35**, 171–173.
Rietveld, H. M. (1969). *J. Appl. Cryst.* **2**, 65–71.
Rodríguez-Carvajal, J. (1993). *Phys. B Condens. Matter*, **192**, 55–69.
Singhal, S. C. (2000). *Solid State Ionics*, **135**, 305–313.
Steele, B. C. H. (2000). *Solid State Ionics*, **129**, 95–110.
Tao, S., Irvine, J. T. S. & Kilner, J. A. (2005). *Adv. Mater.* **17**, 1734–1737.
Tomaszewska, A. & Müller-Buschbaum, Hk. (1993). *Z. Anorg. Allg. Chem.* **619**, 1738–1742.
Troncoso, L., Martínez-Lope, M. J., Alonso, J. A. & Fernández-Díaz, M. T. (2013). *J. Appl. Phys.* **113**, 023511.
Wakeshima, M. & Hinatsu, Y. (2005). *Solid State Commun.* **136**, 499–503.